This manuscript is a non-peer reviewed preprint submitted to *EarthArXiv*.

Periodicity in the Deccan volcanism modulated by plume perturbations at the mid-mantle transition zone

Dip Ghosh[1,2], Joyjeet Sen[1], and Nibir Mandal[1*]

[1]Department of Geological Sciences, Jadavpur University, Kolkata 700032, India

[2]Department of Geology, University of Calcutta, Kolkata 700019, India

Abstract

In peninsular India, the Deccan Traps record massive, continental-scale volcanism in a sequence of magmatic events that mark the mass extinction at the Cretaceous-Paleogene boundary. Although the Deccan volcanism is linked with the Réunion hotspot, the origin of its periodic magmatic pulses is still debated. We develop a numerical model, replicating the geodynamic scenario of the African superplume underneath a moving Indian plate, to explore the mechanism of magmatic pulse generation during the Deccan volcanism. Our model finds a connection between the Réunion hotspot and the African large low shear-wave velocity province (LLSVP) to show the pulse generation from a thermochemical plume in the lower mantle. The plume is perturbed at 660 km, and its head eventually detaches from the tail under the influence of Indian plate movement to produce four major pulses (periodicity: $5 - 8$ Ma), each giving rise to multiple secondary magmatic pulses at a time interval of ~ $0.15 - 0.4$ Ma.

Keywords: Deccan Traps; Cretaceous-Paleogene extinction; Numerical simulation; African LLSVP; Réunion hotspot; Mid-mantle transition.

*Corresponding author (E-mail: nibir.mandal@jadavpuruniversity.in)

1. Introduction

Deccan Traps (DTs), the most spatially extensive continental flood basalt (CFB) province in peninsular India, witness a remarkable event of volcanism in the Earth's Phanerozoic history (Chenet et al., 2009), which in recent times has received particular attention in connection with the mass extinction of biological species (Keller et al., 2012; Wilson, 2014). A school of thought relates this sudden biotic crisis to the enormous volume (> 10^6 km^3) of basaltic magma eruptions in the Deccan provinces (Schoene et al., 2015; Wignall, 2001) during late Mesozoic to early Cenozoic (Fig. 1a). This massive volcanism involved degassing on a global scale, resulting in two significant environmental changes: the first being global warming, carbon cycle disruption, and ocean acidification (Self et al., 2014) associated with volatile emissions, with the second a poisoning of the entire ecosystem (Schmidt et al., 2016) due to SO_2 injection into the upper atmosphere. Another school of thought has proposed a Chicxulub bolide impact theory for the Cretaceous mass extinction (Alvarez et al., 1980; Schulte et al., 2010), but the issue is still debated. The DTs have also stimulated discussions on the long-standing critical question about the origins of large igneous provinces (LIPs) (Campbell & Griffiths, 1990; Dannberg & Sobolev, 2015; C. G. Farnetani & Richards, 1994; Mittal et al., 2021; Mittal & Richards, 2021). What is the potential source of enormous magma supply to LIPs, and how are they connected to lower mantle dynamics (Glišović & Forte, 2017; White & McKenzie, 1995)? This Deccan volcanic province provides an excellent opportunity to study LIPs as it is relatively young and geographically extensive, thus allowing geoscientists to reliably reconstruct the eruption events in space and time.

Based on volcanological and geochemical properties, the Deccan Volcanic Province (DVP) is divided into three principal stratigraphic successions: Kalsubai, Lonavala, and Wai subgroups (Fig. 1b). The volcanic event that defines the Cretaceous-Paleogene boundary (KPB) at 66.043 ± 0.043 Ma (Sprain et al., 2018) occurred $\sim 165 \pm 68$ ka after the emplacement of Kalsubai falls within Khandala, Bushe, or Poladpur Formations (Richards et al., 2015). Using $^{40}K/^{40}Ar$ plagioclase geochronology of erupted basalts and U-Pb geochronology of zircon from intervening ash beds, several workers have constrained the timings of multiple eruption-pulses (Keller et al., 2012; Richards et al., 2015; Schoene et al., 2015, 2019). All these studies agree to a point that the main eruption phases started shortly before the C30n-C29r geomagnetic reversal and ended following the C29r-C29n reversal. Above the KPB, the Wai subgroup consists of geochemically and volcanologically distinct formations, which suggest more voluminous eruptions (Renne et al., 2015; Richards et al., 2015; Sprain et al., 2019).

This study aims to explore the mechanism of unsteady eruption dynamics in the evolution of DVP through multiple pulses, punctuated by quiescent periods. Based on geochemical data, previous studies (Chenet et al., 2007) suggested three phases of DT eruptions, with most of the volume erupted before the KPB, where the second phase is considered responsible for late Cretaceous environmental changes (Chenet et al., 2009; Petersen et al., 2016) (Fig. 1b,c). Alternative views emphasize the Chicxulub impact to propose that the DVP magma eruptions were mostly a post-KPB event (Renne et al., 2015; Richards et al., 2015). More recent investigations from high-precision U-Pb geochronology (Schoene et al., 2019) report three to four discrete pulses during the main eruption event at KPB, each lasting < 100 ka. The first eruption event that formed the lowermost seven formations lasted from ~ 66.3 to 66.15 Ma ago, followed by the second, third, and fourth pulses at ~ 66.1 to 66.0 Ma, ~ 65.9 to 65.8 Ma, and ~ 65.6 to 65.5 Ma to form the Poladpur Formation, the Ambenali Formation, and the uppermost Mahabaleshwar Formation, respectively (Schoene et al., 2019).

A spectrum of geophysical and geochemical studies finds a linkage of the DVP events with the Réunion hotspot (Bredow et al., 2017; Fontaine et al., 2015; Ganerød et al., 2011). Geochemical proxies suggest a link of the source of Deccan basalts to ocean island basalts

(OIB), actively erupting on the La Réunion islands (Peters & Day, 2017). Glisovic et al., (2017) predicted a deep-mantle origin of DVPs from their geophysical model, and proposed a mantle-plume hypothesis to show its connection with the Réunion hotspot. Interestingly, the temporal coincidence of the Deccan volcanic events with the plume-induced accelerated motion of the Indian plate further strengthens this hypothesis (Cande & Stegman, 2011; Glišović & Forte, 2017). Moreover, like Iceland and Tristan da Cunha, the Réunion hotspot is thought to have originated from a laterally vast thermochemical pile above the core-mantle boundary (CMB) beneath present-day Africa, referred to as the African large low shear-wave velocity province (LLSVP) (Mulyukova et al., 2015; Tsekhmistrenko et al., 2021). This pile might have transported primordial materials from CMB to the surface via Réunion and other plumes, as evident from geochemical studies of Sr-Nd-Os systematics (Peters & Day, 2017). Although geophysical and geochemical evidence suggests a connection between the Réunion hotspot and African LLSVP, the mechanism of episodic Deccan volcanism is still unknown.

In this article we examine the thermochemical scenario that favoured the Réunion hotspot to operate in pulsating fashion with characteristic periodicity, producing a huge cumulative volume of Deccan basalt at the KPB. We then show how a single major pulse can give rise to a number of secondary pulses of smaller timescales, as reflected from volcanic episodes in the DVP on time scales less than a million years (Ma). Our thermochemical model allows us to constrain a spectrum of the periodicity timescales (a few Ma to less than a Ma), depending on the thermomechanical properties of the source materials. We also present a budget for the volume-flux from the mantle to the surface.

2. Methods

The thermochemical modeling of Earth's mantle convection has been developed in finite element code ASPECT 2.4.0 (Bangerth et al., 2022b, 2022a; Heister et al., 2017; Kronbichler et al., 2012) , built on deal. II 9.0.1 (Alzetta et al., 2018). This model is used to run thermochemical convections simulations in the framework of Boussinesq approximation, considering mass, momentum, and energy conservation equations:

$$\nabla \cdot \mathbf{u} = 0, \tag{1}$$

$$\nabla P - \nabla \cdot [\mu \dot{\epsilon}] = \Delta \rho g \mathbf{e_z}, \tag{2}$$

$$\rho_0 C_P \left(\frac{\partial T}{\partial t} + \mathbf{u} \cdot \nabla T \right) - \nabla \cdot K \nabla T = \rho_0 H, \tag{3}$$

where $\mathbf{u}$, P, μ, $\dot{\epsilon}$ denote velocity, dynamic pressure, viscosity, and strain rate, respectively. g is the gravitational acceleration, ρ_0 is the reference density of the ambient mantle, C_P is the specific heat at constant pressure, and T, K, and H are the absolute temperature, thermal conductivity, and the internal heating rate, respectively.

To replicate Earth-like convective vigor, we choose a set of parameters to appropriately fix the reference Rayleigh number for the mantle,

$$Ra = \frac{\rho_0 g \alpha_0 \Delta T z^3}{\kappa_0 \mu_0}, \tag{4}$$

α_0, κ_0 and μ_0 represent the reference values of the coefficients of thermal expansion, the thermal diffusivity, and the viscosity of ambient mantle, respectively and ΔT is the temperature difference between the CMB and the surface (values listed in Table 1). The present modeling considers Ra $\sim 10^7$ in most of the cases.

The Discontinuous-Galerkin method (He et al., 2017) is used in ASPECT to track the compositional fields using the advection equation,

$$\frac{\partial \overline{c}}{\partial t} + (\mathbf{u}.\nabla \overline{c}) = 0, \tag{5}$$

where $\overline{c}$ is the compositional vector. The compositional field undergoes advection also in the global flow (Gassmöller et al., 2018), which is tracked by passive tracers (Tackley & King 2003). To maintain a balance, tracer particles are created and destroyed in a simulation run so that at each timestep a cell has a minimum of 60 or a maximum of 100 tracer particles. A cell average interpolation scheme is used in the manipulation of tracers for an arithmetic average of all particle properties in the given cell.

A basal layer of higher density is introduced in the lowermost mantle at a height of 150 km from the CMB to represent the pile material in the model. The density difference between the basal layer and the ambient mantle is expressed by Buoyancy number,

$$B = \frac{\Delta \rho_{\mathrm{c}}}{\rho_0 \alpha_0 \Delta T}, \tag{6}$$

where $\Delta \rho_{\mathrm{c}}$ represents the excess density due to a compositional difference. B expresses the intrinsic density anomaly normalized to that due to thermal expansion. Material properties are calculated from an incompressible *base model* that provides depth-, composition- and temperature-dependent density and viscosity. We use the material model to fix the viscosities assigned for the lithosphere, upper and lower mantle. This model constrains the depth-dependent viscosity $\mu(z)$ as,

$$\mu(z, p, T, \overline{c}, \ldots) = \frac{\mu(z)\mu_b(p, T, \overline{c}, \ldots)}{\mu_0}, \tag{7}$$

a piecewise constant function computed from viscosity pre-factors and transition depths. μ_0 denotes reference viscosity, and

$$\mu_b(p,T,\overline{c}) = \mu_0 H_T \exp\left(-\frac{A(T-T_0)}{T_0}\right)\zeta(\overline{c}), \tag{8}$$

where $\zeta(\overline{c})$ is the compositional pre-factor, A is the thermal viscosity exponent, T_0 is the reference temperature and H_T is a constant implemented in ASPECT (Bangerth et al., 2022a). Assuming the material-density to depend mainly on the thermal expansion and compositional variations, we consider depth-dependent density as,

$$\rho\,(p,T,\overline{c}) = \big(1-\alpha(T-T_0)\big)\rho_0(z) + \Delta\rho_c c_0, \tag{9}$$

α is the coefficient of thermal expansion, $\Delta\rho_c$ is the compositional density difference between the basal layer and the ambient mantle, and c_0 stands for the first component of the compositional vector $\overline{c}$. ρ is calculated from the base model, which also accounts for phase transitions in the ambient mantle and the basal layer (Steinbach & Yuen 1992, Tackley *et al.* 1993). The phase transition is calculated in ASPECT using the phase function approach developed by Richter 1973. The phase function Γ may vary between 0 (pure phase A) and 1 (pure phase B) and represents the relative fraction of phase B. The phase function Γ is implemented in ASPECT using the following equation,

$$\Gamma = 0.5\left(1+\tanh\left(\frac{\Delta p}{w}\right)\right), \tag{10}$$

Where w denotes the phase-transition zone width (Considered to value of 11 km in our model). Δp is the pressure difference across the width of phase transition zones,

$$\Delta p = z - z_{transition} - \gamma(T - T_{transition}), \tag{11}$$

where γ is the Clapeyron slope. $T_{transition}$ for various phase-transitions are obtained in the model from temperature initial conditions. For peridotite, we considered the 410 km (olivine to wadsleyite) and 660 km (ringwoodite to bridgmanite and periclase) phase transitions. The modeling implements pyroxene to garnet and coesite to stishovite phase transformations in the depth range 300 - 400 km that influence the eclogite content of a plume (details in Table 1). We varied the excess-density of the basal layer (pile) from 60 to 140 kg/m^3 (Citron et al., 2020) and its viscosity from 0.1 to 100 times that of the ambient mantle (Fig. S1 a-d). All other parameters are held constant (Table 1). The dynamic topography at the surface is calculated in ASPECT from the stress following Liu & King 2019. The calculations enumerate the stress component (σ_{rr}) that acts in the direction of gravity at the centers of the cells along the top model surface. The dynamic topography (h_{dt}) is then calculated from the relation,

$$h_{dt} = \frac{\sigma_{rr}}{(\mathbf{g}.\mathbf{n})\rho'} \tag{12}$$

where ρ' is the density of the corresponding cell center, and $\mathbf{g}.\mathbf{n}$ is the component of gravity.

To determine the physical properties of sequential plume surges, we consider a line segment across the model box length at a depth of 660 km, which lies above the plume-pulses initiation depth. The excess or deficit of physical properties are obtained from the peak amplitude of the curve with respect to the background value that represents the ambient mantle (Fig. 3b). The plume pulse volume is calculated with respect to the prescribed initial volume (Provided in Table 1) in our models.

The *melting model* implemented in ASPECT by separating the fluid phase from its solid counterpart has been used to evaluate partial melting in the plume pulses. Patrial melting is implemented in ASPECT using a two-phase system where the two phases are related by compaction pressure as,

$$p_c = (1-\phi)(p_s - p_f), \tag{13}$$

where ϕ is the porosity, p_s and p_f denote the solid and the fluid pressures, respectively. The porosity calculations in ASPECT are given in Dannberg & Heister 2016 are identical to Katz *et al.* 2003 formulations. After evaluating the solid velocity (u_s) from stokes equation (Eq. 2), the fluid velocity (u_f) is calculated from Darcy's equation as,

$$u_f = u_s - \frac{K_D}{\phi}\left(\nabla p_f - \rho_f g\right), \qquad (14)$$

K_D is the Darcy coefficient, and ρ_f is fluid density. The porosity is advected using the following relation,

$$\frac{\partial \phi}{\partial t} + u_s \cdot \nabla\phi = \frac{F}{\rho_s} + (1-\phi)\nabla . u_s, \qquad (15)$$

F is the rate of melting. The permeability is then calculated from,

$$k_\phi = k_0\phi^2(1-\phi),^3 \qquad (16)$$

k_0 is the reference permeability.

The 3D model domain covers the entire vertical depth (~ 2890 km) of the mantle with a horizontal length of 11560 km and a width of 4300 km (Fig. S2). The domain is discretized into 5.5 × 5.5 km cells. As this study primarily concerns the dynamics and pulsating nature of the plumes, we consider a pre-existing high-density 150 km thick basal layer (Citron et al., 2020), defined by a single compositional field to represent a thermochemical pile at the CMB (Fig. S1). To initiate a global convection, an initial sinusoidal temperature profile is imposed (Citron et al., 2020; Li et al., 2018) on the background thermal state. In addition, the system is subjected to internal heating within the pile, raising the heating rates up to 20 times that in the background mantle (Fig. S1b).

The top and bottom model-boundaries are subjected to isothermal conditions with *T* = 300K and *T* = 3300K, respectively (Fig. S1c). A uniform velocity condition is imposed at the top boundary of the initial model, keeping all other boundaries under a free-slip condition. We reset the top-layer velocity-boundary condition to accommodate the temporal variation of plate velocity and replicate the plate motion history using the previous model (Seton et al., 2012).

All the model parameters are summarized in Table 1.

To investigate partial melting in a plume, we develop a two-phase model in a 2D Cartesian box, covering a vertical depth of 350 km from Earth's surface and a horizontal distance of 700 km (Fig. S3a, S4). The model dimensions are reduced to achieve a high-resolution analysis of the melting phenomena. Unlike the whole-mantle model, this two-phase modeling accounts for the compressibility of both the solid and the melt phases in the system. The top thermal-boundary layer represents the thermal structure of the Indian shield with a LAB depth of ~160 km corresponding to the Late Mesozoic time. The bottom model boundary is subjected to a thermal perturbation of 250-500 K, reproducing the plume-induced excess temperature (non-adiabatic temperature) obtained from the whole-mantle model (Fig. S3b ii). The boundary velocity condition is the same as in the convection model, except for the bottom boundary, that allows the mass flow in and out, supplying plume materials to generate successive melt pulses. The initial system is considered to be free from porosity. The mesh-deformation techniques of ASPECT are employed to track the surface topography at the upper model boundary in the successive melting events.

3. Results

3.1. Pulsating rise of thermochemical plumes

We consider pile density, viscosity, heat-producing element (HPE) concentration, and major phase transitions in the mantle, as described in Section 2 to obtain a reasonable plume model for the Deccan LIP evolution in the geodynamic framework of the Réunion hotspot. In this modelling, the buoyancy number (B), which measures density contrast of the pile with the ambient lower mantle, accounts for varying relative proportions of eclogite and peridotite within the basal layer (Fig. S5). As the viscosity (μ_b) and HPE concentration of the pile are not well constrained, we varied these two parameters within a plausible range (μ_b: $6 \times 10^{21} - 6 \times 10^{24}$ Pa s and radiogenic heating rate X: 1-20 times of 6×10^{-9} W/m^3) available in the literature (Citron et al., 2020; Dannberg & Sobolev, 2015; Heyn et al., 2020; Li et al., 2018). A uniform velocity-boundary condition is imposed at the upper model boundary to replicate the lithospheric plate kinematics that prevailed during Réunion hotspot activities. The model parameters and boundary conditions are detailed in the Methods section and supplementary Figs. S1, S2.

The plate motion induces a downwelling flow in the mantle, which forces the thermal boundary layer (TBL) at the CMB to pile up laterally and increase its thickness (h_{TBL}~300 km) (Fig. 2a i). The TBL is pushed towards the pile, resulting in further increase of h_{TBL}, that augments the local Rayleigh number in the TBL (Ra_{TBL}) to exceed the critical Ra (Ra_{C}). Its buoyancy eventually becomes strong enough to force the material to flow vertically against the gravity and form a thermochemical plume by entraining a fraction of eclogitic pile materials (Fig. 2a ii). The high-buoyancy enables the plume to grow mainly in the vertical direction within the lower mantle. However, on encounter with the upper mantle, it faces two hindering factors for continuous growth: 1) plate motion effect and 2) eclogite phase transition between 300 and 400 km (Dannberg & Sobolev, 2015). At this stage, the plate-driven flow field that extends to a depth of 660 km exerts strong drags to the plume head (Fig. S6), causing its detachment from the tail counterpart (Fig. 2a iii). However, the buoyancy ultimately takes over the drag to sustain the upward vertical motion of the plume head in the form of a solitary pulse (Fig. 2a iv). Although the ascending head undergoes coesite to stishovite and pyroxene to garnet phase transitions to increase density, its inherent high excess temperatures enable the plume to overcome the density-enhancing barrier to reach the lithosphere-asthenosphere boundary (LAB), where it spreads laterally in the horizontal direction. This stagnation process facilitates thermal mixing and mechanical entrainment within the mantle.

The plume continues to upwell in a pulsating fashion to produce multiple heads (Figs. 2b i-iv), where the primary head gives rise to the first pulse following its detachment from the main body after crossing the 660 km boundary (Fig. 2b i). The plume initiation destabilizes the pile margin (Figs. 2b i, ii), reflected in reducing pile volumes and its high rates of lateral migration (~ 10 km/Ma) (Figs. 3a i, ii), which produces relatively high eclogite proportions (~ 10%) and heat-producing element concentration in the plume (Fig. 3b i). Large buoyancy of the plume head due to its high excess temperature (> 500 K) at the 660 km transition (Dannberg & Sobolev, 2015) and lower density contrast (> -50 kg/m^3) (Figs. 3b ii) facilitates the upward movement that forces the dynamic surface topography to attain a high elevation (~1600 m, Fig. 2b i inset). At this stage, the plume also expands to increase its pulse volume ($\sim 1.5 \times 10^7$ km^3) (Fig. 3a i), and at the same time dissipates its heat to the surrounding, lowering the excess temperature to ~ 300 K (Fig. S7) to reduce its buoyancy , as found from petrological data (Herzberg & Gazel, 2009) and other numerical model estimates (C. G. Farnetani, 1997; Cinzia G. Farnetani & Samuel, 2005; Samuel & Bercovici, 2006) for LIP formation. This thermal change eventually arrests the upward motion of plume and directs it to spread laterally beneath the lithosphere-asthenosphere boundary (LAB).

The pile margin remains unstable, causing a large volume of material to upwell through the plume tail to produce a second pulse (Fig. 2b ii), allowing new materials to accumulate in a threshold volume at 660 Km. Unlike the first pulse, the second pulse evolves with a moderate amount of eclogite and heat-producing elements (HPE) to form significantly lower pulse volumes (0.9×10^7 km^3) (Fig. 3a i) and dynamic topography (~800 m) (Fig. 2b ii inset) due to a lower excess temperature (~ 400 K) at the 660 km boundary and density contrast (> -40 kg/m^3) (Figs. 3b ii). The pile progressively moves further away from the plume axis, but with a reducing rate (~5-6 km/Ma). It sustains the periodic material supply to the 660 km boundary to produce tertiary pulses (Figs. 2b iii, iv). The pile eventually attains a stable state; this unstable to stable transition results in a drastic reduction in material supply to the plume (Fig. 3a i), marked by a further lowering in pulse volume ($\sim 0.5 \times 10^7$ km^3). This pulse has a low excess temperature (~ 250 K) at 660 km boundary and density contrast (~-20 kg/m^3) (Fig. 3b i-ii), manifested in weak positive dynamic topography (~100-200 m) (Figs. 2b iii, iv insets).

Although all the sequential pulses ultimately reach the LAB and contribute to melt production and subsequent volcanism, the primary (first) pulse takes the lead role in forming the LIPs due to its large excess temperature (> 500K) at the 660 km boundary (Fig. S7) and volume ($\sim 1.5 \times 10^7$ km^3). The thermochemical pile, which is the primary material feeder to the pulses, fulfills a specific set of physio-chemical parameters to generate a large melt-volume and dynamic topography required for Deccan LIP formation. Previous model-estimates (Citron et al., 2020) and various geophysical studies (Harris & McNutt, 2007; Sleep, 1990) showed high peaks in the surface heat flow during LIP and CFB events and their subsequent decay with time (Fig. S8).

The present model simulations suggest that a strong poloidal motion in the mantle developed as a consequence of the subduction that forced the pile to move in the southward direction at a significant rate. This finding agrees with the inferences from other studies that claimed the southward movement of African LLSVP due to the presence of deep-mantle southward poloidal flow associated with the Tethyan subduction event over the past 130 Ma (Hassan et al., 2020). To carry out a parametric analysis of this phenomenon, we considered a 2D model-domain to represent a north-south cross-section of the Indian plate tectonic configuration in late Mesozoic and Cenozoic (past 130 Ma), reconstructing the eastern flank of the African LLSVP relative to the Indian subcontinent (Fig. S2).

3.2. Buoyancy effects on plume rise dynamics

We investigated the effects of pile buoyancy (B) on the pulse generation process at the mid-mantle transition zone for a given viscosity ratio (μ ~1) and HPE concentration. For low B values ($<$ 1), the mantle flow efficiently drags the pile horizontally to widen the exposed CMB fraction, causing both h_{TBL} and pile height (h_{pile}) to increase at high rates (Figs. 4 a-d; 5a). Consequently, the pile becomes unstable to accelerate material flux into the plume, and gives rise to initial pulses with large volumes ($> 1.5 \times 10^7$ km^3) (Fig. 5b) and high dynamic topography (> 1500 m) (Figs. 4 a, b inset). Increasing B weakens the interaction of mantle flow with the pile due to a high intrinsic density of the basal layer, leading to TBL thickening at slow rates (Figs. 4 e-h). As a result, the plume having the same initial excess temperature produces pulses of much smaller volumes ($< 1.1 \times 10^7$ km^3) (Fig. 5b) and low dynamic topography (<1100 m) (Figs. 4 e, f insets). Moreover, the volume differences in primary, secondary, and tertiary pulses become more pronounced at low B values (Fig. 5b).

3.3. Viscosity effects on pulse-driven processes

Geophysical studies suggest that the viscosity of thermochemical piles can go up to 1000 times higher than that of the ambient mantle (Heyn et al., 2020; Kellogg & King, 1997). We find that an increase in the viscosity ratio (μ) from 1 to 100 considerably dampens the vertical growth of piles to facilitate their stability under a given B and HPE concentration (Fig. 4 c-d, g-h), reflected in the lower rates of pile-volume changes (Fig. 5c). This increase of μ, on the other hand, strengthens the mantle flow-pile interaction, as evident from large exposed CMB areas (Fig. 5a), which promotes horizontal shortening of the pile at the cost of its vertical growth, eventually to reduce pulse volumes by up to 12 % (Fig. 5b) and amplify the time periodicity of pulse generation. μ also significantly influences the dynamic topography. The model estimates for $\mu = 1$ yield an unusually high dynamic topography (> 3000 m) for low B values (< 0.8), which can be considered unrealistic for thermochemical plumes. Increasing μ to 100 lowers the topographic elevation < 2000 m, which can be correlated with Deccan volcanic events.

3.4. Effect of internal heat production on plume dynamics

Geochemical observations on OIBs support the presence of enriched mantle reservoirs as mantle heterogeneity and/or variable mantle reservoirs (Peters & Day, 2017). Some of these sources are less degassed and hence, are more enriched in HPEs. One possibility is that such reservoirs could be present within LLSVPs since they are primarily composed of primordial materials, subducted Hadean crust, or recycled oceanic crustal remnants from a decomposed subducted plate (Deschamps et al., 2011). Previous estimates, based on heat budget calculations, show that the heat-producing element concentrations (c_{HPE}) can be as high as 20 to 25 times that of the background mantle (Citron et al., 2020). To study the role of this factor on the pile dynamics, we increased c_{HPE} of the pile by up to 20 times that of the ambient lower mantle. Plumes that originate from the pile edges entrain HPE-enriched pile materials to increase its excess temperature. However, c_{HPE} has relatively weak effects, as compared to other parameters, such as viscosity ratio (μ) (Figs. 4 b, d and f, h,). c_{HPE} primarily influences the dynamic topography and, more importantly, the material supply to thermochemical plumes (Figs. 5b, c). Increase in c_{HPE} amplifies the dynamic topography and also enhances material supply to the plume, especially at a lower buoyancy (B). The other remarkable effect of c_{HPE} on plume geometry is that the plume develops a thick tail, which facilaites pile material transport to the mid-mantle region in larger volumes (Fig. 4d), compared to that produced in a lower c_{HPE} condition. This effect is also evident from reduction in pile volumes with time (Fig. 5c), which implies a more effective pile material entrainment into the plume tail. In addition, high c_{HPE} enables the plume to gain a large excess temperature that results in dynamic topography with a realistic elevation of ~1600 m for the primary pulse when μ = 100 (Fig. 4d inset).

The parametric analyses described in the preceding sections lead us to reconstruct a field diagram that delineate the physical conditions of plume growth in three primary modes (Fig. 5e). Low B and μ yield continuous plumes from an unstable pile, which transform into pulsating plumes with increasing B and μ as they exceed threshold values. A further increase in B causes the pile to become stable, allowing only thermal plumes to grow without any pile material. Increasing c_{HPE} has a counter effect to B, switching a transition to pulsating plumes at high c_{HPE}.

3.5. Melt transport from a thermochemical plume

The Indian shield (a stable craton) had a thickness of 150-200 km before it started to interact with the Reunion plume (Naganjaneyulu & Santosh, 2012), implying a deep upper thermal-boundary layer. Depending upon the initial temperature, composition, and volume of the plume head, our thermochemical model suggests that the onset of melting in the plume occurred at a depth of ~ 150 to 250 km. To study the melting behaviour, we focus on the melting process in the primary plume head obtained from the thermochemical model. As the plume head approaches the LAB, the plume temperature exceeds the local solidus to initiate the melting process. The degree of partial melting, calculated from the model using Eq. A4 is found to be $< 5\%$. This melting increases the porosity, which in turn enhances permeability in the plume head (Fig. S4), allowing the melts to percolate by Darcy flow and cause melt enrichment (as high as $\sim 20\%$) preferentially in the top region of the plume head (Fig. S9). Earlier studies have predicted similar melt enrichment in mantle plumes (Herzberg & Gazel, 2009; Katz et al., 2003).

During the initial phase of pulse ascent, the magnitudes of melt and plume velocities lie compatibly in a range of $0.4 - 0.6\ \mathrm{m/year}$ (Fig. S3b i), but as the pulse ascends to a shallower depth, the melts owing to their lower density (2700 kg/m^3), gain a higher velocity (> 1.2 m/year) to segregate from the plume materials at the LAB (Fig. S3b v). Our model results suggest that the melt-ascent velocity is directly proportional to the porosity in the system, which increases steadily with the plume evolution. Unlike the plume head, the segregated melts always ascend nearly in a vertical direction, implying that the plate velocity hardly affects the upward melt flow dynamics. At a depth of ~60-80 km, the segregated melts start to spread laterally, forming a melt pool beneath the lithosphere (a permeability barrier) (Fig. 6a). The melt front interacts with the lithosphere to produce horizontal shear that sets in small-scale downwelling, leading to thinning of the TBL. Upwelling of the melt front within the lithosphere ultimately gives rise to volcanism. We evaluated the melt volume, velocity, time scale of the melt rise, and dynamic topography as a function of the initial plume volume, temperature, and density, which are presented in Fig. 6 and Fig. S3b.

Since the primary plume pulse has the highest volume (~1.5×10^7 km^3), it contains a high concentration of HPEs. This condition, aided with a high excess temperature (~500 K) at the 660 km boundary, enables the pulse to overcome the upper-mantle buoyancy barriers. Model observations indicate that the higher excess temperatures and HPE concentrations result in a greater melting depth (~250 km) of the initial pulse (Fig. 6a i), and also enhance the excess buoyancy that accelerates the upward flow of melts to reach a depth of 50 km within 150-180 kyr (Fig. 6b). The porosity evolution, coupled with a high excess temperature, facilitates melt generation during the plume ascent to produce an enormous melt-volume ($\sim 0.28 \times 10^6$km^3)

at the LAB (Fig. 6b). The melt pool then efficiently incorporates lithospheric materials by thermal erosion to increase the melt-volume further ($\sim 0.35 \times 10^6$km^3), ultimately giving rise to massive volcanism. Following this melt pulse generation, the plume head is then significantly depleted in HPE concentration. Secondly, the heat dissipation to the ambient mantle lowers the excess temperature (~300 K) in the plume. The thermal change by these mechanisms relocates the melting depth at a shallower level (150 to 180 km) during the subsequent pulses, where a moderate excess temperature with a relatively low HPE concentration and a smaller pulse volume set in the upward melt flows at slow rates ($\sim$ 0.5 m/year), taking up to 300 kyr to reach the LAB. These second-generation pulses reduce their melt-volumes to $< 0.2 \times 10^6$ km^3. In addition, the thermal erosion of the lithosphere at LAB by the melt pools becomes less effective and fails to substantially increase the melt volumes (Fig. 6a ii). Thus, they produced erupted volumes significantly lower than that produced in the first pulse. The smaller pulses are manifested in relatively low topographic elevations (Figs. 6b, c). The tertiary melt pulses further reduce their volumes and their excess temperatures (~ 250 K) and lose their capacity for large-scale thermal erosion of the lithosphere and attain a stagnation state at a depth of ~50 km (Fig. 6a iii).

4. Discussion

4.1. Deccan volcanism - African superplume connection

It is now a well-accepted hypothesis that the existence of African LLSVP dates back to at least the Pangea event (Zhang et al., 2010). During the Gondwana-proto-Laurussia convergence, several cold subducting slabs assembled in the lower mantle beneath the African continental lithosphere to form this distinct layer above the CMB, whose current location and shape have been framed in the post-Pangea subduction history. Recent mantle convection models coupled to continuously evolving plate boundaries (Hassan et al., 2016; Müller et al., 2016) track the African LLSVP positions through time, considering the subduction driven mantle flow due to Neo-Tethys Ocean closure, as illustrated in Fig. 7a, b. The model results suggest that the western margin of African LLSVP remained almost stable during the entire Cretaceous period, but the eastern flank has continuously relocated its position. The time-dependent effect of subduction on the north (closure of Tethys) produced a strong southward lower-mantle poloidal flow (Fig. 7a), leading to mantle upwelling in the south. The upwelling dynamics, in turn, induced a convective mantle "roll" that forced the eastern flank of the African LLSVP boundary to migrate southward and the Indian plate to move northward at a higher velocity (Cande & Stegman, 2011; Glišović & Forte, 2017). These interpretations are further validated by geophysical observations that predict deformation and southward movement of the African LLSVP under east Africa (Ford & Long, 2015).

The poloidal flow obtained in our model (Fig. 2a) resulted in a thermal instability within the exposed CMB on the north of the LLSVP, which subsequently migrated towards the African LLSVP and amplified the pile at its eastern flank to attain a thickness of ~800-1000 km (Fig. 2b ii). The laterally migrating TBL instabilities climbed up the pile edge to reach the crest and finally formed a mature plume. The positional reconstruction of the African LLSVP and the Indian plate for this time period allows us to conclude that the eastern flank of African LLSVP coincided with the Indian plate location in a time frame of 70-65 Ma (Fig. 7b). This plume then generated successive pulses upon reaching the mid-mantle transition zone through the late Mesozoic and Cenozoic, where the first pulse corresponds to the Deccan events at 66 Ma. The plume initiation decelerated the southward pile migration to ~ 6-7 km/Ma (Fig. 7c ii) because the plume forced pile materials to effectively upwell in the vertical direction. Subsequently, the pile migrated further south-westward, whereas the Indian plate had north-eastward movement.

The plume continued to form periodically the secondary and tertiary pulses at mid-mantle depth at an interval of 5-8 Ma, giving rise to successive eruptions from the Réunion hotspot. The plume process eventually reduced pulse volumes and involved a sharp change in the chemical characteristics of the Réunion lava flows during the post-Deccan volcanism period (Peters & Day, 2017). With time, the eastern margin of pile shifted its position further southwest to reach its current location (Fig. 7b). The present model suggests that the process of sequential plume-head detachment at the mid-mantle transition zone modulated the periodic pulse generation to determine the time scale, volume, and topography associated with each of these pulses. Considering a CMB temperature of $3300\,\mathrm{K}$ and an initial pile thickness of $150\ \mathrm{km}$, the model results for B in a range $0.8 - 1.0$ yield a periodicity of 5-8 Ma, similar to that of Réunion activity throughout the Cenozoic. To tally the dynamic topography, the pile also needs to be ~ 100 times viscous ($\mu{\sim}100$) and ~ 20 times HPE enriched than the ambient lower mantle. This condition produces a primary pulse volume of $14 - 15.5 \times 10^6\ \mathrm{km}^3$ and dynamic topography of ~ 2000 m related to the Deccan event, followed by the next generation of pluses with volumes of $\sim 12 \times 10^6\ \mathrm{km}^3$, $\sim 7 \times 10^6\ \mathrm{km}^3$, $\sim 3.5 \times 10^6\ \mathrm{km}^3$ (Fig. 5b) and topography of ~ 1400 m, ~ 700 m, and ~ 200 m (Fig. 2b insets).

4.2. The Deccan volcanic periodicity

To study the time periodicity of Deccan volcanism, we focus on the melting process in the primary plume head obtained from our thermochemical model (Fig. 6; Fig. S3). The model results suggest that the plume head locally underwent melting within the asthenosphere to produce in three eruptive events within a time scale of 1 Ma, where the first event occurred within 0.15 Ma from the plume head stagnation with a cumulative volume of $0.32 \times 10^6\ \mathrm{km}^3$ (Fig. 6b), correlated with the lowermost seven formations produced during the period ~ 66.5-

66.3 Ma. The second event took place after a quiescent period of ~ 0.3 Ma with a volume of 0.18×10^6 km^3, which corresponds to the ~ 66.0 Ma Poladpur Formation. Finally, the third pulse that initiated after 0.4 Ma produced a volume of 0.15×10^6 km^3, which can be equated with the Ambanali and later formations deposited during ~ 65.6-65.3 Ma. Based on these model calculations, we estimate a volume flux of ~8-9 km^3/year for the first event, subsequently reduced to $\sim 5 - 5.5$ km^3/year and $\sim 4 - 4.5$ km^3/year, for the second and third events, respectively. This estimate implies that the rate of Deccan volcanic eruption in a pulse (time scale ≤ 100 Ka) exceeded the global value (3 to 4 km^3/year) by a factor of 1.5 to 3. Moreover, there must be hiatuses in the order of tens of thousands of kiloyears within the pulses to balance the total volume estimates. Geochemical proxies also suggest a sharp increase of mantle contributions to later volcanic formations, such as Poladpur and Ambenali, indicating a reduction of magma-crust interface area (Renne et al., 2015). The higher rates of thermal erosion at the LAB during the first two events effectively thinned the lithosphere and weakened the vigorous crust-mantle interaction during the subsequent melt pulse events, as revealed from our models (Fig. 6a).

Although the model estimates broadly agree with the time gaps between different episodes of the Deccan volcanism, they somewhat underestimate the erupted volumes predicted from petrological and geochemical studies (Schoene et al., 2019). Groups of flows within the Poladpur and Mahabaleshwar Formations, each potentially comprising > 50,000 km^3, lack any secular variation of paleomagnetic poles, suggesting the eruption at high rates, ~ 1000 km^3/year on decadal to centuries scales. Our volume and flux estimates for eruptions prior to the KPB tally well with the available data; however, they do not account for either the high melt volumes or the rate of eruption for the post-KPB eruptions. We thus hypothesize that there was a transition in the nature of volcanism across the KPB, the explanation of which demands the possible effects of other internal or external factors. One possible explanation could be that the Chicxulub bolide impact accelerated the eruption rates, as suggested by the previous workers (Renne et al., 2015).

4.3. Comparison with major global LIP events

We will now discuss the Deccan volcanism that occurred sequentially in three major pulses in the context of similar episodic volcanic events from other LIPs and hotspots, such as Hawaii, Réunion, Yellowstone and others (Morrow & Mittelstaedt, 2021). They show the periodicity of their volcanic events on varied timescales (Fig. 8). For example, the Hawaii-Emperor hotspot track records a sequence of magmatic pulses at around 64 Ma, 50 Ma, 42 Ma, and 28 Ma, implying a pulsating time scale of about 10 Ma (Van Ark & Lin, 2004). On the other hand, from bathymetry analysis Wessel (2016) has established a much shorter pulsating time scale (< 2 Ma) for the post-22 Ma volcanism, as observed in the Deccan volcanism. The Yellowstone LIP started its volcanism at around 18 Ma (Schutt et al., 2008), followed by two distinct magmatic peak events at around 11 Ma and 5 Ma (Stachnik et al., 2008; Waite et al., 2006). In a recent study of the Yellowstone super-volcano the tomographic P-wave model has detected hot pulses in the upper mantle (Huang et al., 2015). These discrete bodies, most probably pockets of partial melts, represent episodic pulses produced by a large plume source in the mantle, as predicted from our numerical model simulations (Fig. 6a). The Réunion hotspot displays a major emplacement in Deccan traps at 66-68 Ma, with later magmatic peaks at 57 Ma, 48 Ma, 35 Ma, 8 Ma, and 2 Ma (Mjelde et al., 2010).

4.4. Model limitations

The model presented here treats the lithosphere as an upper thermal boundary layer, which does not account for visco-plastic rheology with a failure criterion, which is a limitation in our simulations. Secondly, the creep processes that are often activated in the upper mantle could influence the shape and the ascent rate of the plume head, which are not explored in this study. In addition, our primary model excludes any compressibility effect of the solid phases. The plume melting models consider a reaction time scale of 10^3 years due to computational constraints. This might overshoot the overall timescale of melting and melt migration.

5. Summary and Conclusions

The thermochemical model simulations demonstrate that the following parameters: pile-ambient mantle viscosity ratio (μ), buoyancy number (B), and heat-producing element concentration (c_{HPE}) have controlled the Réunion hotspot dynamics and its connection to the seismically observed African LLSVP. The position of India is found to match with the African LLSVP location at the end of the Cretaceous Period, where the LLSVP acted as the source of the Réunion hotspot materials to produce the Deccan LIP and subsequent eruption events.

We show that an instability in the TBL above the CMB played a critical role in the Reunion hotspot formation. The instability initiated on the eastern flank of the African LLSVP during the Neo-Tethys subduction (130-150 Ma), but migrated to the pile crest to form a plume. The plume ascent was perturbed at the mid-mantle transition zone to produce four major pulses on a time interval of 5-8 Ma. The model calculations suggest that, at the onset time (Late Cretaceous) of Réunion Hotspot volcanism, the African LLSVP had a Buoyancy number (B) in the range of $0.8 - 1.0$, pile-ambient mantle viscosity ratio (μ) in the order of 100 and heat-producing element concentration (c_{HPE}) 20 times that of the ambient lower mantle. The primary pulse of the Réunion plume had thereby sufficient volumes ($> 1.5 \times 10^7$ km^3) and excess temperature (> 500 K) at the 660 km transition to produce the Deccan LIPs. The partial-melting model envisages that the primary pulse subsequently gave rise to 3 melt pulses with volumes in the order of ~ $0.15 - 0.35 \times 10^6$ km^3 at a time interval of $0.15 - 0.4$ Ma, as recorded in the Deccan traps.

Finally, we conclude that most of the LIPs evolve in pulses on characteristic time scales, modulated by a combined action of the pile processes operating at the CMB and the feeding mechanism into the plume stem, modulated by a mid-mantle perturbation. The entire sequence of pulses is divided into two categories: major pulses with a periodicity of 5-8 Ma, determined by the plume-head detachment at the mid-mantle transition zone, and minor melt pulses with a 0.15-0.4 Ma time periodicity, determined by the melting phenomenon within each major pulse. The temporal variations in magma eruption characteristics are consistent with depth-dependent compositional heterogeneity of the plume source.

Acknowledgments

The present work has been supported by the DST-SERB through the J. C. Bose fellowship (SR/S2/JCB-36/2012) to NM and an INSPIRE faculty fellowship (DST/INSPIRE/04/2022/002647) granted by Department of Science and Technology (DST), India, to DG. The Computational Infrastructure for Geodynamics (geodynamics.org), funded by the National Science Foundation under awards EAR-0949446 and EAR-1550901 is acknowledged for supporting the development of ASPECT. D.G. and J.S. are thankful to Juliane Dannberg for insightful discussions. We especially thank Dr. Simon Gatehouse, BHP who critically read an earlier version of this manuscript and provided many constructive suggestions.

Data Availability Statement

The model parameters required to produce the results are given in Table 1 and Table 2 and the supplementary information file. The relevant data for Fig. 5 are provided in the repository (https://doi.org/10.6084/m9.figshare.24203859). The simulation code is freely available online under the terms of the GNU General Public License at https://github.com/geodynamics/aspect.

References

Alvarez, L., Alvarez, W., Asaro, F., & Michel, H. V. (1980). Extraterrestrial Cause for the Cretaceous-Tertiary Extinction. *Science*, *208*(4448), 1095–1108.

Alzetta, G., Arndt, D., Bangerth, W., Boddu, V., Brands, B., Davydov, D., et al. (2018). The deal.II library, Version 9.0. *Journal of Numerical Mathematics*, *26*(4), 173–183. https://doi.org/10.1515/jnma-2018-0054

Van Ark, E., & Lin, J. (2004). Time variation in igneous volume flux of the Hawaii-Emperor hot spot seamount chain. *Journal of Geophysical Research: Solid Earth*, *109*(11), 1–18. https://doi.org/10.1029/2003JB002949

Bangerth, W., Dannberg, J., Fraters, M., Gassmoeller, R., Glerum, A., Heister, T., et al. (2022a). Advanced Solver for Problems in Earth's ConvecTion, User Manual. https://doi.org/10.6084/m9.figshare.4865333

Bangerth, W., Dannberg, J., Fraters, M., Gassmoeller, R., Glerum, A., Heister, T., et al. (2022b). ASPECT v2.4.0. Zenodo. https://doi.org/10.5281/zenodo.6903424

Bredow, E., Steinberger, B., Gassmöller, R., & Dannberg, J. (2017). How plume-ridge interaction shapes the crustal thickness pattern of the Réunion hotspot track. *Geochemistry, Geophysics, Geosystems*, *18*(8), 2930–2948. https://doi.org/10.1002/2017GC006875

Campbell, I. H., & Griffiths, R. W. (1990). Implications of mantle plume structure for the evolution of flood basalts. *Earth and Planetary Science Letters*, *99*(1–2), 79–93. https://doi.org/10.1016/0012-821X(90)90072-6

Cande, S. C., & Stegman, D. R. (2011). Indian and African plate motions driven by the push force of the Réunion plume head. *Nature*, *475*(7354), 47–52. https://doi.org/10.1038/nature10174

Chenet, A. L., Quidelleur, X., Fluteau, F., Courtillot, V., & Bajpai, S. (2007). 40K-40Ar dating of the Main Deccan large igneous province: Further evidence of KTB age and short duration. *Earth and Planetary Science Letters*, *263*(1–2), 1–15. https://doi.org/10.1016/j.epsl.2007.07.011

Chenet, A. L., Courtillot, V., Fluteau, F., Gérard, M., Quidelleur, X., Khadri, S. F. R., et al. (2009). Determination of rapid Deccan eruptions across the Cretaceous-Tertiary boundary using paleomagnetic secular variation: 2. Constraints from analysis of eight new sections and synthesis for a 3500-m-thick composite section. *Journal of Geophysical Research: Solid Earth*, *114*(6). https://doi.org/10.1029/2008JB005644

Citron, R. I., Lourenço, D. L., Wilson, A. J., Grima, A. G., Wipperfurth, S. A., Rudolph, M. L., et al. (2020). Effects of Heat-Producing Elements on the Stability of Deep Mantle Thermochemical Piles. *Geochemistry, Geophysics, Geosystems*, *21*(4), 1–17. https://doi.org/10.1029/2019GC008895

Crameri, F., Shephard, G. E., & Heron, P. J. (2020). The misuse of colour in science communication. *Nature Communications*, *11*(1), 1–10. https://doi.org/10.1038/s41467-020-19160-7

Dannberg, J., & Heister, T. (2016). Compressible magma/mantle dynamics: 3-D, adaptive simulations in ASPECT. *Geophysical Journal International*, *207*(3), 1343–1366. https://doi.org/10.1093/gji/ggw329

Dannberg, J., & Sobolev, S. V. (2015). Low-buoyancy thermochemical plumes resolve controversy of classical mantle plume concept. *Nature Communications*, *6*, 1–9. https://doi.org/10.1038/ncomms7960

Deschamps, F., Kaminski, E., & Tackley, P. J. (2011). A deep mantle origin for the primitive signature of ocean island basalt. *Nature Geoscience*, *4*(12), 879–882. https://doi.org/10.1038/ngeo1295

Farnetani, C. G. (1997). Excess temperature of mantle plumes: The role of chemical stratification across D″. *Geophysical Research Letters*, *24*(13), 1583–1586. https://doi.org/10.1029/97GL01548

Farnetani, C. G., & Richards, M. A. (1994). Numerical investigations of the mantle plume initiation model for flood basalt events. *Journal of Geophysical Research*, *99*(B7). https://doi.org/10.1029/94jb00649

Farnetani, Cinzia G., & Samuel, H. (2005). Beyond the thermal plume paradigm. *Geophysical Research Letters*, *32*(7), 1–4. https://doi.org/10.1029/2005GL022360

Fontaine, F. R., Barruol, G., Tkalčić, H., Wölbern, I., Rümpker, G., Bodin, T., & Haugmard, M. (2015). Crustal and uppermost mantle structure variation beneath La Réunion hotspot track. *Geophysical Journal International*, *203*(1), 107–126. https://doi.org/10.1093/gji/ggv279

Ford, H. A., & Long, M. D. (2015). A regional test of global models for flow, rheology, and seismic anisotropy at the base of the mantle. *Physics of the Earth and Planetary Interiors*, *245*, 71–75. https://doi.org/10.1016/j.pepi.2015.05.004

Ganerød, M., Torsvik, T. H., van Hinsbergen, D. J. J., Gaina, C., Corfu, F., Werner, S., et al. (2011). Palaeoposition of the seychelles microcontinent in relation to the deccan traps and the plume generation zone in late cretaceous-early palaeogene time. *Geological Society Special Publication*, *357*(1), 229–252. https://doi.org/10.1144/SP357.12

Gassmöller, R., Lokavarapu, H., Heien, E., Puckett, E. G., & Bangerth, W. (2018). Flexible and Scalable Particle-in-Cell Methods With Adaptive Mesh Refinement for Geodynamic Computations. *Geochemistry, Geophysics, Geosystems*, *19*(9), 3596–3604. https://doi.org/10.1029/2018GC007508

Glišović, P., & Forte, A. M. (2017). On the deep-mantle origin of the Deccan Traps. *Science*, *355*(6325), 613–616. https://doi.org/10.1126/science.aah4390

Harris, R. N., & McNutt, M. K. (2007). Heat flow on hot spot swells: Evidence for fluid flow. *Journal of Geophysical Research: Solid Earth*, *112*(3), 1–14. https://doi.org/10.1029/2006JB004299

Hassan, R., Müller, R. D., Gurnis, M., Williams, S. E., & Flament, N. (2016). A rapid burst in hotspot motion through the interaction of tectonics and deep mantle flow. *Nature*, *533*(7602), 239–242. https://doi.org/10.1038/nature17422

Hassan, R., Williams, S. E., Gurnis, M., & Müller, D. (2020). East African topography and volcanism explained by a single, migrating plume. *Geoscience Frontiers*, *11*(5), 1669–1680. https://doi.org/10.1016/j.gsf.2020.01.003

He, Y., Puckett, E. G., & Billen, M. I. (2017). A discontinuous Galerkin method with a bound preserving limiter for the advection of non-diffusive fields in solid Earth geodynamics. *Physics of the Earth and Planetary Interiors*, *263*, 23–37. https://doi.org/10.1016/j.pepi.2016.12.001

Heister, T., Dannberg, J., Gassmöller, R., & Bangerth, W. (2017). High accuracy mantle convection simulation through modern numerical methods - II: Realistic models and problems. *Geophysical Journal International*, *210*(2), 833–851. https://doi.org/10.1093/gji/ggx195

Herzberg, C., & Gazel, E. (2009). Petrological evidence for secular cooling in mantle plumes. *Nature*, *458*(7238), 619–622. https://doi.org/10.1038/nature07857

Heyn, B. H., Conrad, C. P., & Trønnes, R. G. (2020). How Thermochemical Piles Can (Periodically) Generate Plumes at Their Edges. *Journal of Geophysical Research: Solid Earth*, *125*(6). https://doi.org/10.1029/2019JB018726

Huang, H., Lin, F., Schmandt, B., Farrell, J., Smith, R. B., & Tsai, V. C. (2015). The Yellowstone magmatic system from the mantle plume to the upper crust. *Science*, *348*(6236), 773–776.

Kale, V. S., & Pande, K. (2022). Reappraisal of Duration and Eruptive Rates in Deccan Volcanic Province, India. *Journal of the Geological Society of India*, *98*(1), 7–17. https://doi.org/10.1007/s12594-022-1921-5

Kale, V. S., Bodas, M., Chatterjee, P., & Pande, K. (2020). Emplacement history and evolution of the Deccan Volcanic Province, India. *Episodes*, *43*(1), 278–299. https://doi.org/10.18814/EPIIUGS/2020/020016

Katz, R. F., Spiegelman, M., & Langmuir, C. H. (2003). A new parameterization of hydrous mantle melting. *Geochemistry, Geophysics, Geosystems*, *4*(9), 1–19. https://doi.org/10.1029/2002GC000433

Keller, G., Adatte, T., Bhowmick, P. K., Upadhyay, H., Dave, A., Reddy, A. N., & Jaiprakash, B. C. (2012). Nature and timing of extinctions in Cretaceous-Tertiary planktic foraminifera preserved in Deccan intertrappean sediments of the Krishna-Godavari Basin, India. *Earth and Planetary Science Letters*, *341–344*, 211–221. https://doi.org/10.1016/j.epsl.2012.06.021

Kellogg, L. H., & King, S. D. (1997). The effect of temperature dependent viscosity on the structure of new plumes in the mantle: Results of a finite element model in a spherical, axisymmetric shell. *Earth and Planetary Science Letters*, *148*, 13–26.

Kronbichler, M., Heister, T., & Bangerth, W. (2012). High accuracy mantle convection simulation through modern numerical methods. *Geophysical Journal International*, *191*(1), 12–29. https://doi.org/10.1111/j.1365-246X.2012.05609.x

Li, M., Zhong, S., & Olson, P. (2018). Linking lowermost mantle structure, core-mantle boundary heat flux and mantle plume formation. *Physics of the Earth and Planetary Interiors*, *277*, 10–29. https://doi.org/10.1016/j.pepi.2018.01.010

Liu, S., & King, S. D. (2019). A benchmark study of incompressible Stokes flow in a 3-D spherical shell using ASPECT. *Geophysical Journal International*, *217*(1), 650–667. https://doi.org/10.1093/gji/ggz036

Mittal, T., & Richards, M. A. (2021). The Magmatic Architecture of Continental Flood Basalts: 2. A New Conceptual Model. *Journal of Geophysical Research: Solid Earth*, *126*(12). https://doi.org/10.1029/2021JB021807

Mittal, T., Richards, M. A., & Fendley, I. M. (2021). The Magmatic Architecture of Continental Flood Basalts I: Observations From the Deccan Traps. *Journal of Geophysical Research: Solid Earth*, *126*(12), 1–54. https://doi.org/10.1029/2021JB021808

Mjelde, R., Wessel, P., & Müller, R. D. (2010). Global pulsations of intraplate magmatism through the Cenozoic. *Lithosphere*, *2*(5), 361–376. https://doi.org/10.1130/L107.1

Morrow, T. A., & Mittelstaedt, E. L. (2021). Quantifying Periodic Variations in Hotspot Melt Production. *Journal of Geophysical Research: Solid Earth*, *126*(7). https://doi.org/10.1029/2021JB021726

Müller, R. D., Seton, M., Zahirovic, S., Williams, S. E., Matthews, K. J., Wright, N. M., et al. (2016). Ocean Basin Evolution and Global-Scale Plate Reorganization Events since Pangea Breakup. *Annual Review of Earth and Planetary Sciences*, *44*, 107–138. https://doi.org/10.1146/annurev-earth-060115-012211

Mulyukova, E., Steinberger, B., Dabrowski, M., & Sobolev, S. V. (2015). Survival of LLSVPs for billions of years in a vigorously convecting mantle: Replenishment and destruction of chemical anomaly. *Journal of Geophysical Research: Solid Earth*, *120*(5), 3824–3847. https://doi.org/10.1002/2014JB011688

Naganjaneyulu, K., & Santosh, M. (2012). The nature and thickness of lithosphere beneath the Archean Dharwar Craton, southern India: A magnetotelluric model. *Journal of Asian Earth*

Sciences, *49*, 349–361. https://doi.org/10.1016/j.jseaes.2011.07.002

Peters, B. J., & Day, J. M. D. (2017). A geochemical link between plume head and tail volcanism. *Geochemical Perspectives Letters*, *5*, 29–34. https://doi.org/10.7185/geochemlet.1742

Petersen, S. V., Dutton, A., & Lohmann, K. C. (2016). End-Cretaceous extinction in Antarctica linked to both Deccan volcanism and meteorite impact via climate change. *Nature Communications*, *7*(May), 1–9. https://doi.org/10.1038/ncomms12079

Renne, P. R., Sprain, C. J., Richards, M. A., Self, S., Vanderkluysen, L., & Pande, K. (2015). State shift in Deccan volcanism at the Cretaceous-Paleogene boundary, possibly induced by impact. *Science*, *350*(6256), 76–78.

Richards, M. A., Alvarez, W., Self, S., Karlstrom, L., Renne, P. R., Manga, M., et al. (2015). Triggering of the largest Deccan eruptions by the Chicxulub impact. *Bulletin of the Geological Society of America*, *127*(11–12), 1507–1520. https://doi.org/10.1130/B31167.1

Richter, F. M. (1973). Finite Amplitude Convection Through a Phase Boundary. *Geophysical Journal of the Royal Astronomical Society*, *35*(1–3), 265–276. https://doi.org/10.1111/j.1365-246X.1973.tb02427.x

Ritsema, J., Deuss, A., Van Heijst, H. J., & Woodhouse, J. H. (2011). S40RTS: A degree-40 shear-velocity model for the mantle from new Rayleigh wave dispersion, teleseismic traveltime and normal-mode splitting function measurements. *Geophysical Journal International*, *184*(3), 1223–1236. https://doi.org/10.1111/j.1365-246X.2010.04884.x

Samuel, H., & Bercovici, D. (2006). Oscillating and stagnating plumes in the Earth's lower mantle. *Earth and Planetary Science Letters*, *248*(1–2), 90–105. https://doi.org/10.1016/j.epsl.2006.04.037

Schmidt, A., Skeffington, R. A., Thordarson, T., Self, S., Forster, P. M., Rap, A., et al. (2016). Selective environmental stress from sulphur emitted by continental flood basalt eruptions. *Nature Geoscience*, *9*(1), 77–82. https://doi.org/10.1038/ngeo2588

Schoene, B., Samperton, K. M., Eddy, M. P., Keller, G., Adatte, T., Bowring, S. A., et al. (2015). U-Pb geochronology of the Deccan Traps and relation to the end-Cretaceous mass extinction. *Science*, *347*(6218), 182–184. https://doi.org/10.1126/science.aaa0118

Schoene, B., Eddy, M. P., Samperton, K. M., Keller, C. B., Keller, G., Adatte, T., & Khadri, S. F. R. (2019). U-Pb constraints on pulsed eruption of the Deccan Traps across the end-Cretaceous mass extinction. *Science*, *363*(6429), 862–866. https://doi.org/10.1126/science.aau2422

Schulte, P., Alegret, L., Arenillas, I., Arz, J. A., Barton, P. J., Bown, P. R., et al. (2010). The chicxulub asteroid impact and mass extinction at the cretaceous-paleogene boundary. *Science*, *327*(5970), 1214–1218. https://doi.org/10.1126/science.1177265

Schutt, D. L., Dueker, K., & Yuan, H. (2008). Crust and upper mantle velocity structure of the Yellowstone hot spot and surroundings. *Journal of Geophysical Research: Solid Earth*, *113*(3), 1–14. https://doi.org/10.1029/2007JB005109

Self, S., Schmidt, A., & Mather, T. A. (2014). Emplacement characteristics, time scales, and volcanic gas release rates of continental flood basalt eruptions on Earth. *Special Paper of the Geological Society of America*, *505*(16), 319–337. https://doi.org/10.1130/2014.2505(16)

Seton, M., Müller, R. D., Zahirovic, S., Gaina, C., Torsvik, T., Shephard, G., et al. (2012). Global continental and ocean basin reconstructions since 200Ma. *Earth-Science Reviews*, *113*(3–4), 212–270. https://doi.org/10.1016/j.earscirev.2012.03.002

Sleep, N. H. (1990). Hotspots and mantle plumes: some phenomenology. *Journal of Geophysical Research*, *95*(B5), 6715–6736. https://doi.org/10.1029/JB095iB05p06715

Sprain, C. J., Renne, P. R., Clemens, W. A., & Wilson, G. P. (2018). Calibration of chron C29r: New high-precision geochronologic and paleomagnetic constraints from the Hell Creek region, Montana. *Bulletin of the Geological Society of America*, *130*(9–10), 1615–1644. https://doi.org/10.1130/B31890.1

Sprain, C. J., Renne, P. R., Vanderkluysen, L., Pande, K., Self, S., & Mittal, T. (2019). The eruptive tempo of deccan volcanism in relation to the cretaceous-paleogene boundary. *Science*, *363*(6429), 866–870. https://doi.org/10.1126/science.aav1446

Stachnik, J. C., Dueker, K., Schutt, D. L., & Yuan, H. (2008). Imaging Yellowstone plume-lithosphere interactions from inversion of ballistic and diffusive Rayleigh wave dispersion and crustal thickness data. *Geochemistry, Geophysics, Geosystems*, *9*(6). https://doi.org/10.1029/2008GC001992

Steinbach, V., & Yuen, D. A. (1992). The effects of multiple phase-transitions on Venusian mantle convection. *Geophysical Research Letters*, *19*(22), 2243–2246.

Tackley, P J, Stevenson, D. J., Glatzmaier, G. A., & Schubert, G. (1993). Effects of an endothermic phase transition at 670 km depth on spherical mantle convection. *Nature*, *361*, 699–704.

Tackley, Paul J., & King, S. D. (2003). Testing the tracer ratio method for modeling active compositional fields in mantle convection simulations. *Geochemistry, Geophysics, Geosystems*, *4*(4), 1–15. https://doi.org/10.1029/2001GC000214

Tsekhmistrenko, M., Sigloch, K., Hosseini, K., & Barruol, G. (2021). A tree of Indo-African mantle plumes imaged by seismic tomography. *Nature Geoscience*, *14*(8), 612–619. https://doi.org/10.1038/s41561-021-00762-9

Waite, G. P., Smith, R. B., & Allen, R. M. (2006). VP and VS structure of the Yellowstone hot spot from teleseismic tomography: Evidence for an upper mantle plume. *Journal of Geophysical Research: Solid Earth*, *111*(4), 1–21. https://doi.org/10.1029/2005JB003867

White, R. S., & McKenzie, D. (1995). Mantle plumes and flood basalts. *Journal of Geophysical Research*, *100*(B9). https://doi.org/10.1029/95jb01585

Wignall, P. B. (2001). Large igneous provinces and mass extinctions. *Earth Science Reviews*, *53*(1–2), 1–33. https://doi.org/10.1016/S0012-8252(00)00037-4

Wilson, G. P. (2014). Mammalian extinction, survival, and recovery dynamics across the Cretaceous-Paleogene boundary in northeastern Montana, USA. *Special Paper of the Geological Society of America*, *503*(15), 365–392. https://doi.org/10.1130/2014.2503(15)

Zhang, N., Zhong, S., Leng, W., & Li, Z. X. (2010). A model for the evolution of the Earth's mantle structure since the Early Paleozoic. *Journal of Geophysical Research: Solid Earth*, *115*(6), 1–22. https://doi.org/10.1029/2009JB006896

Figure Captions:

Fig. 1. Geology of the Deccan volcanic province (DVP). **(a)** Map showing the four main sub-provinces of DVP. The Deccan traps (DTs) rest on Precambrian basement rocks (shown in various legend patterns). The terrain contains a number of structural zones, such as lineaments and escarpment (marked as green dashed lines). Blue lines depict the major rivers flowing across DVP. WGE = Western Ghat Escarpment, EGMB = Eastern Ghat Mobile Belt. Reconstructed from (Kale et al., 2020; Kale & Pande, 2022) **(b)** Stratigraphic succession of the DVP (Left column) and their corresponding cumulative eruption volumes (Right column) along with ages for the three main subgroups of DVP in the Western Ghats (Renne et al., 2015). The panel shows the following elements (from left to right): cumulative stratigraphic height, geological time scale with the KPB indicated by the gray area, timescale of geomagnetic polarity with various magnetic chrons, and cumulative volume of Deccan lava. It also includes the probabilistic volumetric eruption rate and the Chicxulub impact time from Schoene et al., 2019 **(c)** A thematic geological cross-section of the DTs to illustrate the three major phases and their corresponding formations (Chenet et al., 2009). Color legends correspond to those used in (b).

Fig. 2. (a) Evolution of a thermochemical plume in the 3D reference model (buoyancy number: B = 0.8, viscosity ratio: μ = 100 and heat producing element concentration (c_{HPE}) same as the background mantle): (i) Piling up of TBL due to forcing by a downwelling flow in mantle, leading to growth of a rudimentary instability on the extreme right side of the TBL, followed by lateral advection and climb of the instability to the pile crest, (ii) Development of a mature plume from the instability, (iii) Perturbation of the plume head at the mid-mantle transition zone to produce a primary pulse. Note that the pulse in the upper mantle undergoes deflection to the right under the influence of plate velocity, and (iv) Sequential formation of multiple pulses with time by mid-mantle perturbation. (b) Pulsating ascent dynamics of a thermochemical plume at the mid-mantle transition zone: Development of successive four pulses (i-iv) from the thermochemical plume. Colors (Crameri et al., 2020) represent the temperature and dashed yellow lines delineate the pile margin. Insets show the dynamic topography (in km) corresponding to each pulse in the panels. The horizontal dimension of the insets correspond to 5000 km around the location of the pulse.

Fig. 3 (a) Calculated plots of **(i)** the pulse and the pile volumes and **(ii)** varying locations of the plume (black) and the pile margin (yellow) during the four pulse events (denoted in different colors), obtained from the reference model. The volumes are calculated based on the initial volume of the basal layer provided in Table 1. **(b)** Horizontal variation of the physico-chemical properties in four successive plume pulses produced at the mid-mantle transition. The graphical plots correspond to a depth of 660 km. (i) Variations of excess temperature showing a maximum peak value (>500K) for the first pulse (yellow curve). Note that the next pulses consistently reduce their peak values. The secondary pulse (Brown) also has a high excess temperature but they are subsequently weakend with the tertiary pulses (blue and green curves).

Their reducing trend indicate less entrainment of pile materials by the plume. (ii) Density profiles showing the first pulse with the highest negative density anomaly, reflecting strong buoyancy head. The density anomalies significantly weaken in the secondary and tertiary pulses.

Fig. 4. Effects of the model parameters on plume-pulse and pile dynamics**.** Geometry and locations of the pulses generated from a plume head and the pile in different models with varying parameters: **(a)-(d)** B = 0.8, and **(e)** - **(h)** B = 1.2. Viscosity ratio: μ = 1 to 100 in the vertical direction and heat producing elements concentration: c_{HPE} = 1X to 20X (where X denote c_{HPE} value for the background mantle) in the horizontal direction. Color scale is same as in Fig. 2. Inset of each figure shows the dynamic topography (in km) at the surface for the pulses presented in the respective snapshot. The horizontal dimension of the insets correspond to 5000 km around the location of the pulse.

Fig. 5. Calculated plots from numerical models of successive pulses for different parametric values. (**a**) Variation in the exposed fraction of the core mantle boundary (CMB) for different model parameters. **(b)** - **(c)** Decreasing trends of successive pulse and pile volumes. **(d)** Varying plume head locations for successive pulses. The x-axis represents successive pulses, which in turn reflect progressive time. The symbols stand for the parameter B, and the colors denote μ and c_{HPE}. Their details are provided in the legend. **(e)** A regime diagram of the various modes of thermochemical plume growth as a function of buoyancy number (B) and viscosity ratio (μ).

Fig. 6. Melt production by partial melting of plume head in the model. (**a**) Melt localization in three successive melt pulses (**i-iii**) at lithosphere-asthenosphere boundary (LAB). They originate from a single major pulse obtained from the whole mantle model. Colors represent the temperature and the colored contours represent melt fraction. Black line delineates the deformed LAB geometry. The slight tilt in the plume axis results from plate movement. The first two pulses (i-ii) involve intense thermal erosion at the contact between the melt front and the LAB, resulting in thinning of the thermal boundary layer. The top boundary is deflected to produce topography during the successive melting events. **(b)** Calculated plots of melt volume formed in successive melt pulses. **(c)** Melt-driven dynamic topography for three successive pulses. The colors used to represent the pulses in (b) and (c) are shown in the legend.

Fig. 7. African LLSVP and its connection to the Réunion hotspot and the Deccan volcanism. (**a**) Global map showing the present-day location of African LLSVP (gray shade) and the poloidal velocity components at a level 150 km above CMB constructed from Ford and Long, 2015. Strong south-westward velocity can be noticed at the eastern flank of the LLSVP. **(b)** Contours of 75% chemical concentration corresponding to a time series, 100 Ma to present day. The contour plots depict positional changes of African LLSVP through geologic time. The contours are redrawn from Hassan et al., 2016, 2020 expect that for 66 Ma (dashed contour) which is interpolated. The figure also shows location of the Tethyan subduction system and

Indian plate (yellow) during the Deccan volcanism at 66 Ma. At this time the western margin of Indian plate was located directly above the eastern flank of the African LLSVP. The base map has been produced using S40RTS (Ritsema et al., 2011) depth slice at 2800 km on SubMachine. **(c)** Plots of the locations of African LLSVP (solid lines), Réunion plume tail (dotted lines) and plume head (dashed lines) **(i)**, the rate of southward migration of LLSVP, and **(ii)** those calculated from two of our representative models (see text) for each successive pulsation events.

Fig. 8. A timescale analysis of the global LLSVP related volcanic events. Histogram analysis of the periodic variations of volcanism in Hawai'i (Blue), Réunion (Saffron), and Yellowstone (Green). Short-term (< 1.5-2 Ma oscillations) and long-term (> 3 Ma oscillations) temporal variations are distinct in the plots (see discussion).

Figure 1

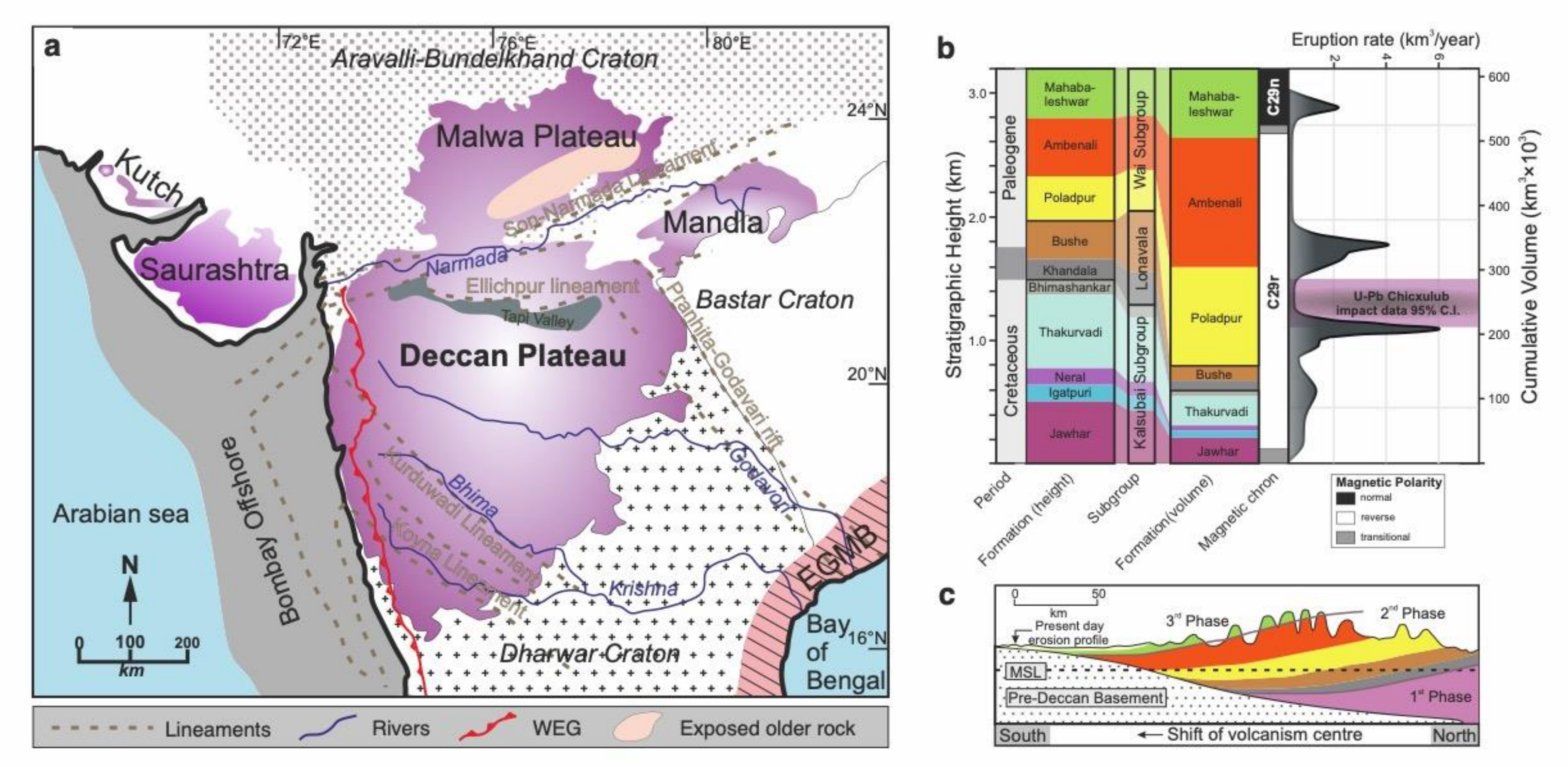
a
72°E
76°E
80°E
24°N
20°N
16°N
Aravalli-Bundelkhand Craton
Malwa Plateau
Son-Narmada Lineament
Mandla
Kutch
Saurashtra
Narmada
Ellichpur lineament
Tapi Valley
Bastar Craton
Pranhita-Godavari rift
Deccan Plateau
Arabian sea
Bombay Offshore
Bhima
Kurduwadi Lineament
Koyna Lineament
Godavari
Krishna
Dharwar Craton
EGMB
Bay of Bengal
N
0 100 200
km
Lineaments
Rivers
WEG
Exposed older rock
b
Eruption rate (km³/year)
Stratigraphic Height (km)
Cumulative Volume (km³×10³)
Paleogene
Cretaceous
Mahabaleshwar
Ambenali
Poladpur
Bushe
Khandala
Bhimashankar
Thakurvadi
Neral
Igatpuri
Jawhar
Wai Subgroup
Lonavala
Kalsubai Subgroup
C29n
C29r
U-Pb Chicxulub impact data 95% C.I.
Period
Formation (height)
Subgroup
Formation(volume)
Magnetic chron
Magnetic Polarity
normal
reverse
transitional
c
0 50
km
Present day erosion profile
3rd Phase
2nd Phase
1st Phase
MSL
Pre-Deccan Basement
South
Shift of volcanism centre
North

Figure 2

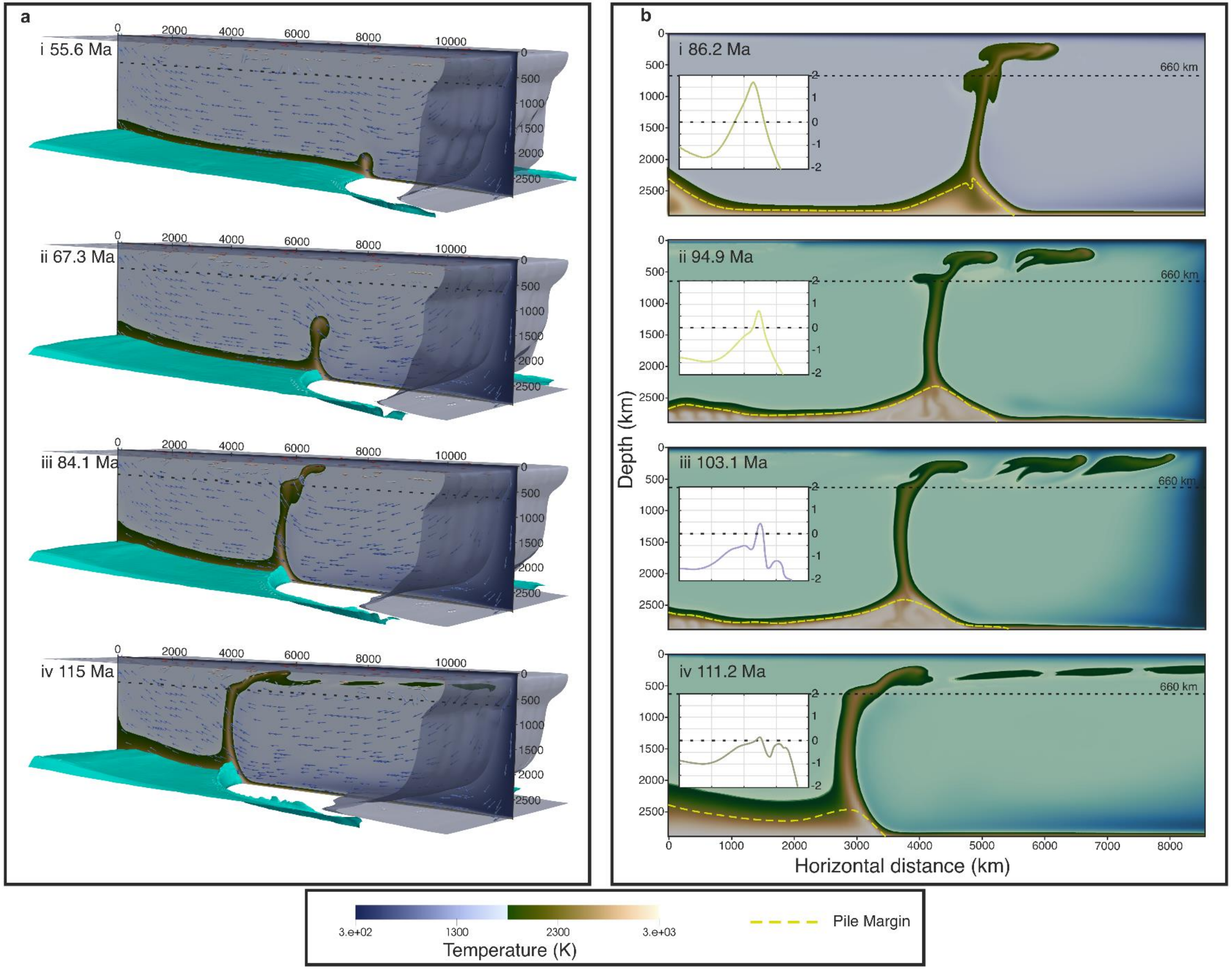

a
i 55.6 Ma
ii 67.3 Ma
iii 84.1 Ma
iv 115 Ma
0
2000
4000
6000
8000
10000
500
1000
1500
2000
2500
b
i 86.2 Ma
ii 94.9 Ma
iii 103.1 Ma
iv 111.2 Ma
660 km
Depth (km)
Horizontal distance (km)
0
1000
2000
3000
4000
5000
6000
7000
8000
3.e+02
1300
2300
3.e+03
Temperature (K)
Pile Margin

881

Figure 3

882

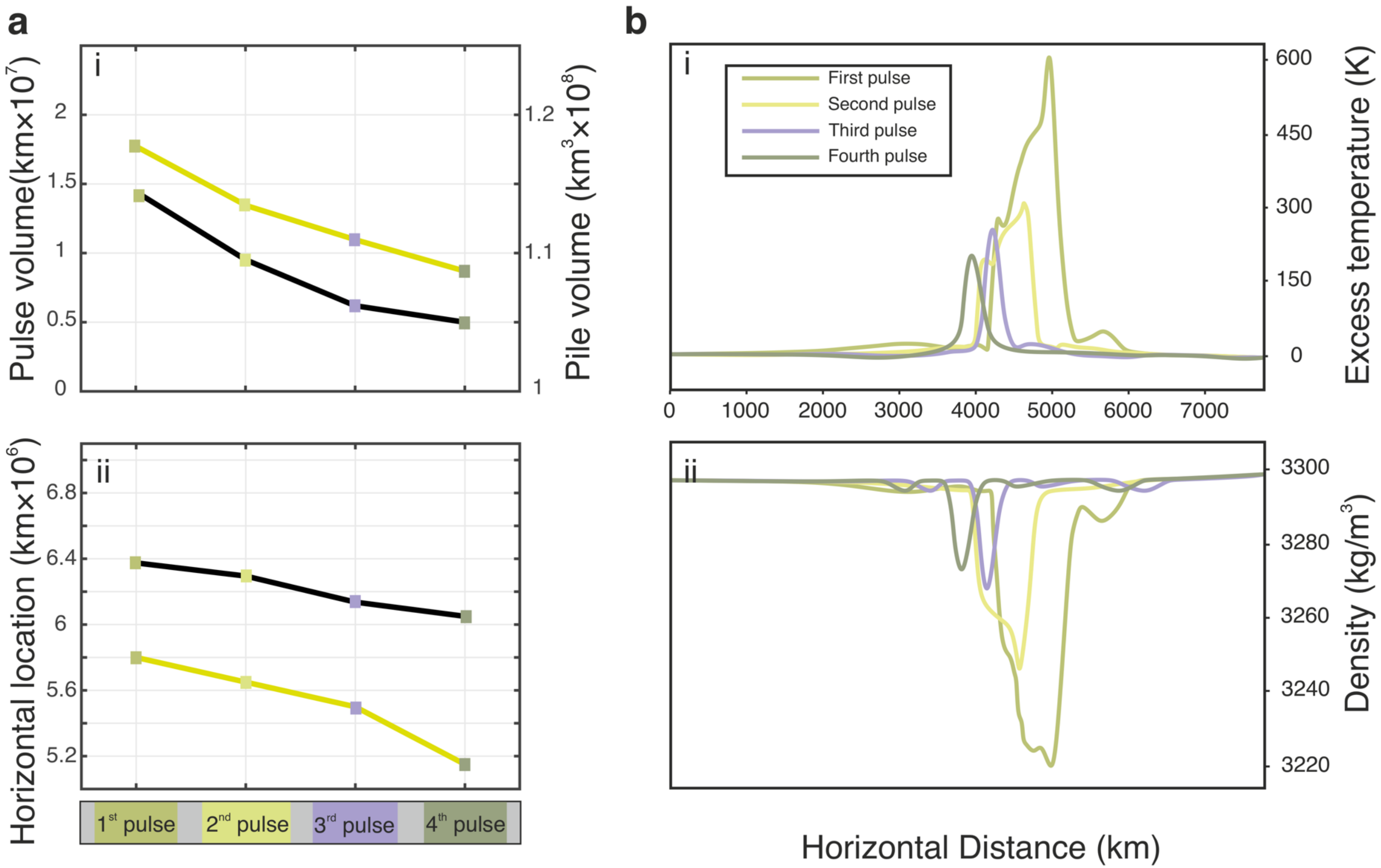

883 **Figure 4**

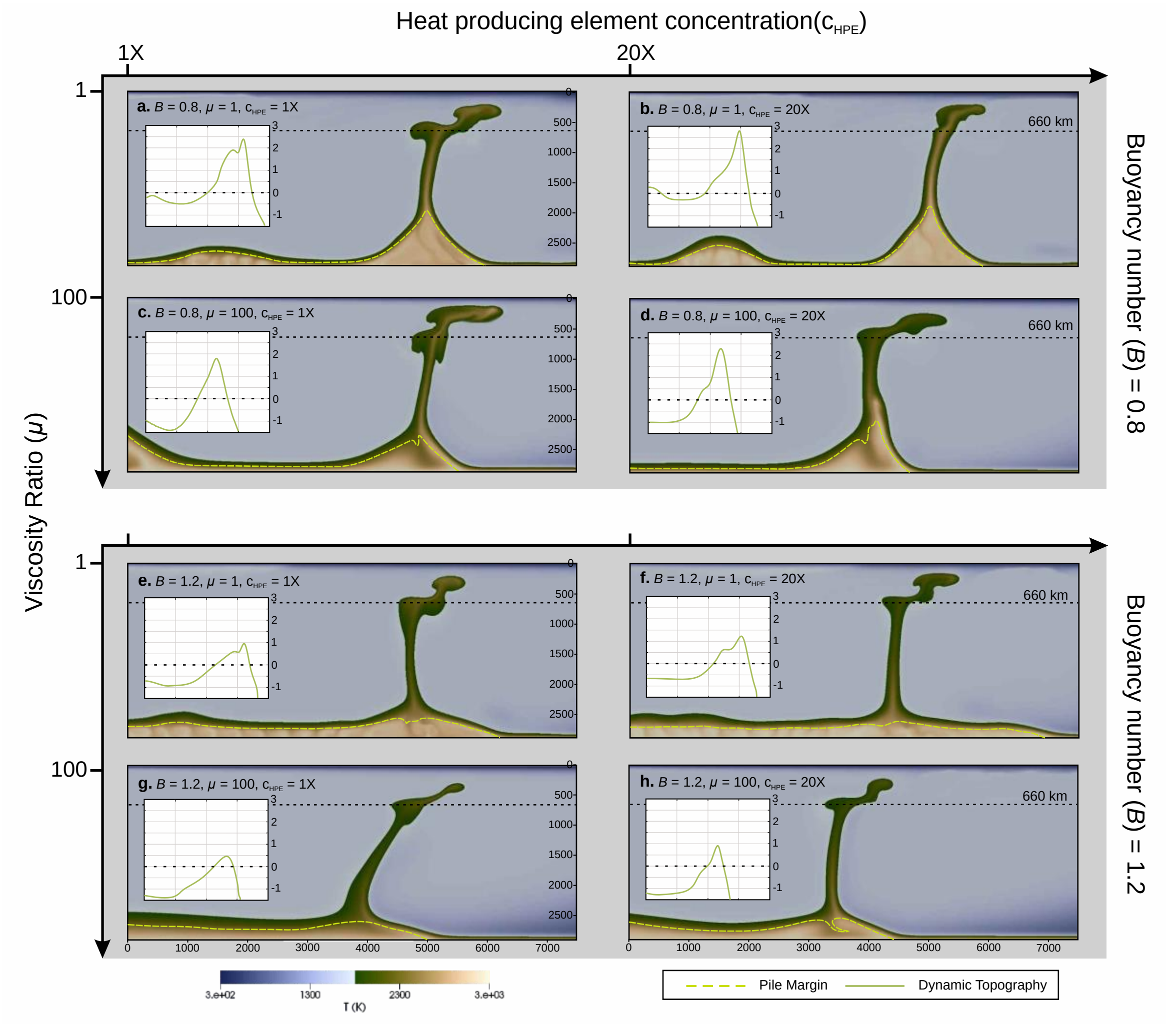

884

Figure 5

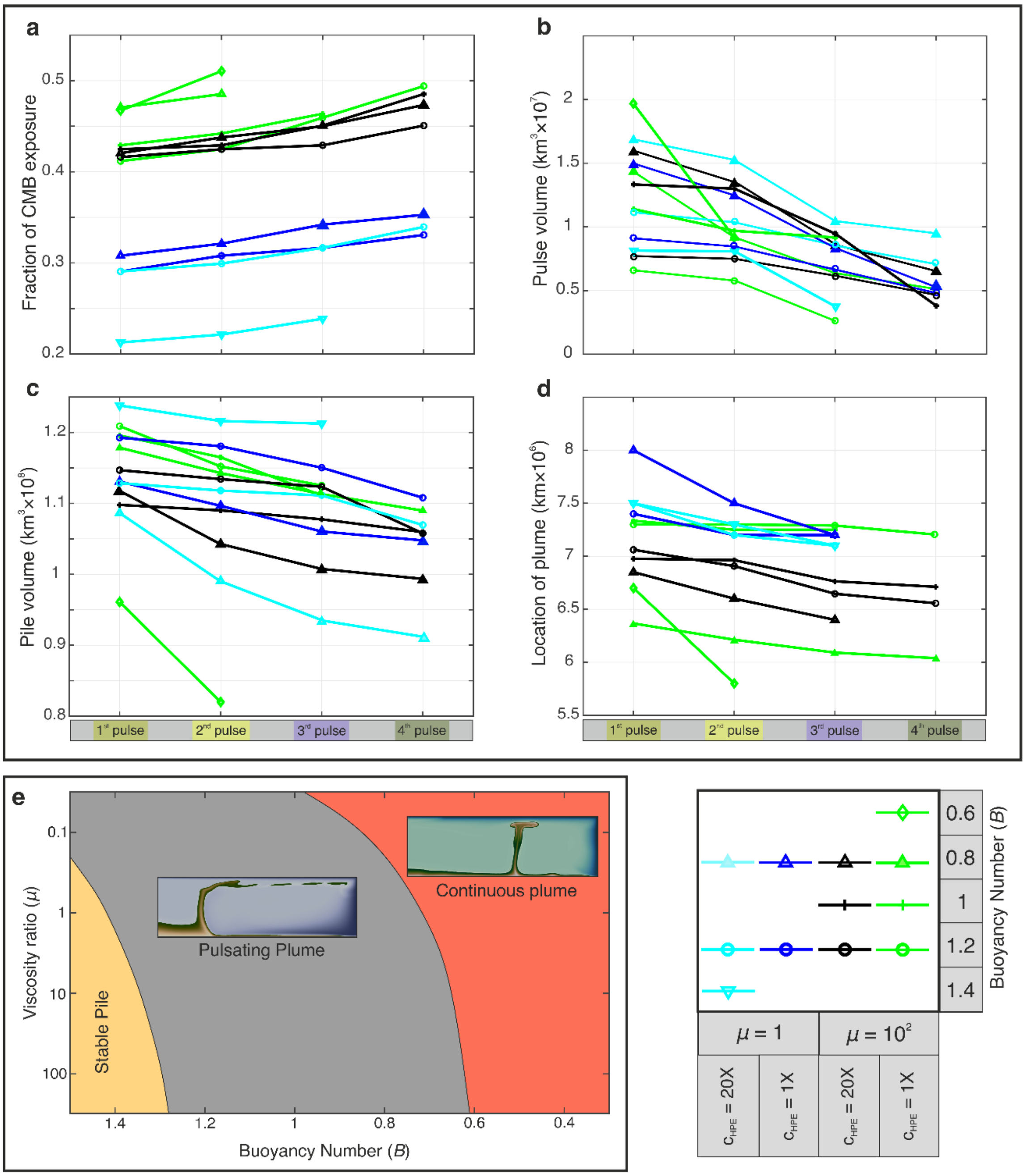

a
Fraction of CMB exposure
b
Pulse volume (km³×10⁷)
c
Pile volume (km³×10⁸)
d
Location of plume (km×10⁶)
1st pulse
2nd pulse
3rd pulse
4th pulse
e
Viscosity ratio (μ)
Buoyancy Number (B)
Stable Pile
Pulsating Plume
Continuous plume
0.6
0.8
1
1.2
1.4
Buoyancy Number (B)
μ = 1
μ = 10²
c_HPE = 20X
c_HPE = 1X
c_HPE = 20X
c_HPE = 1X

887

Figure 6

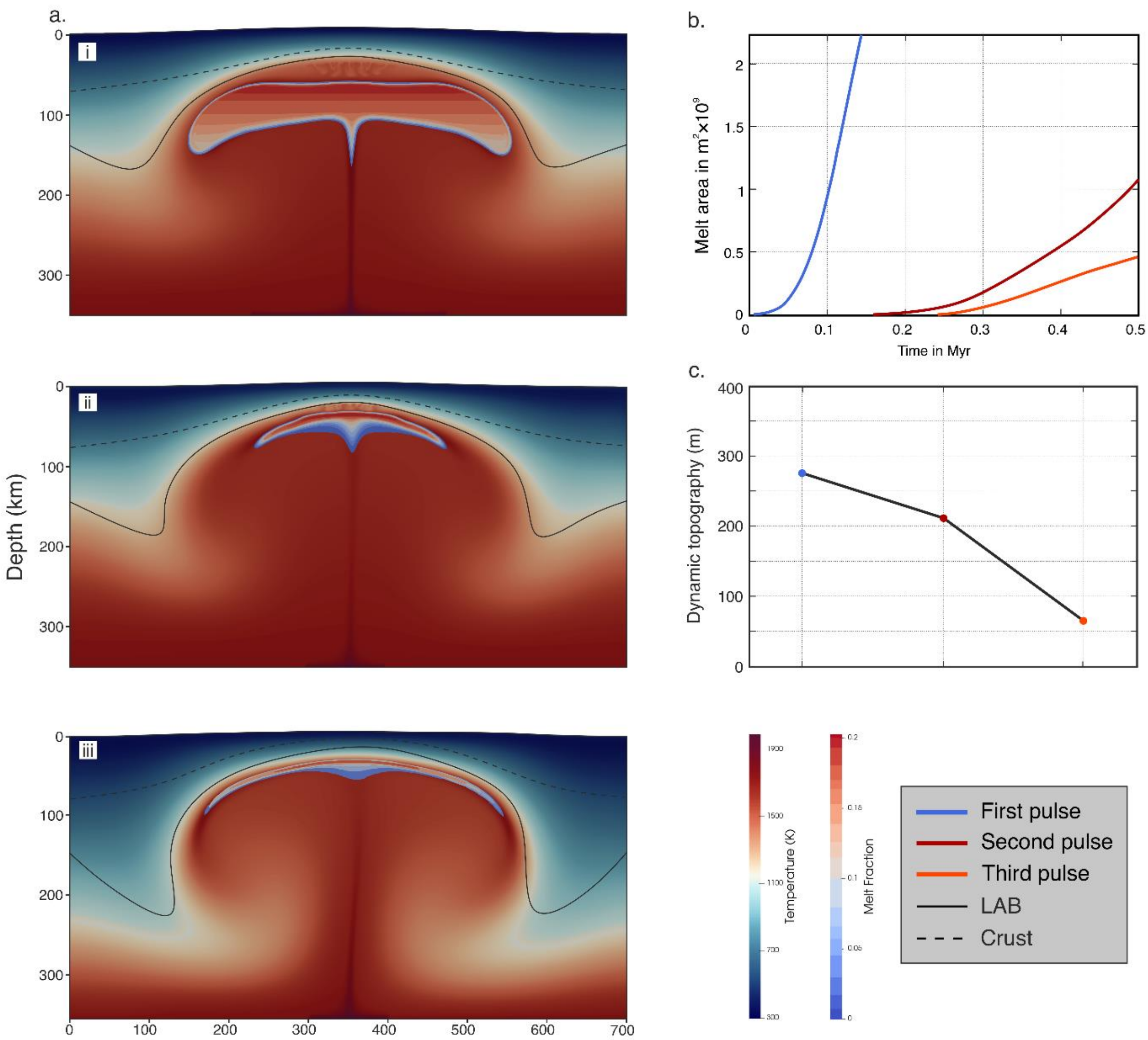

888

Figure 7

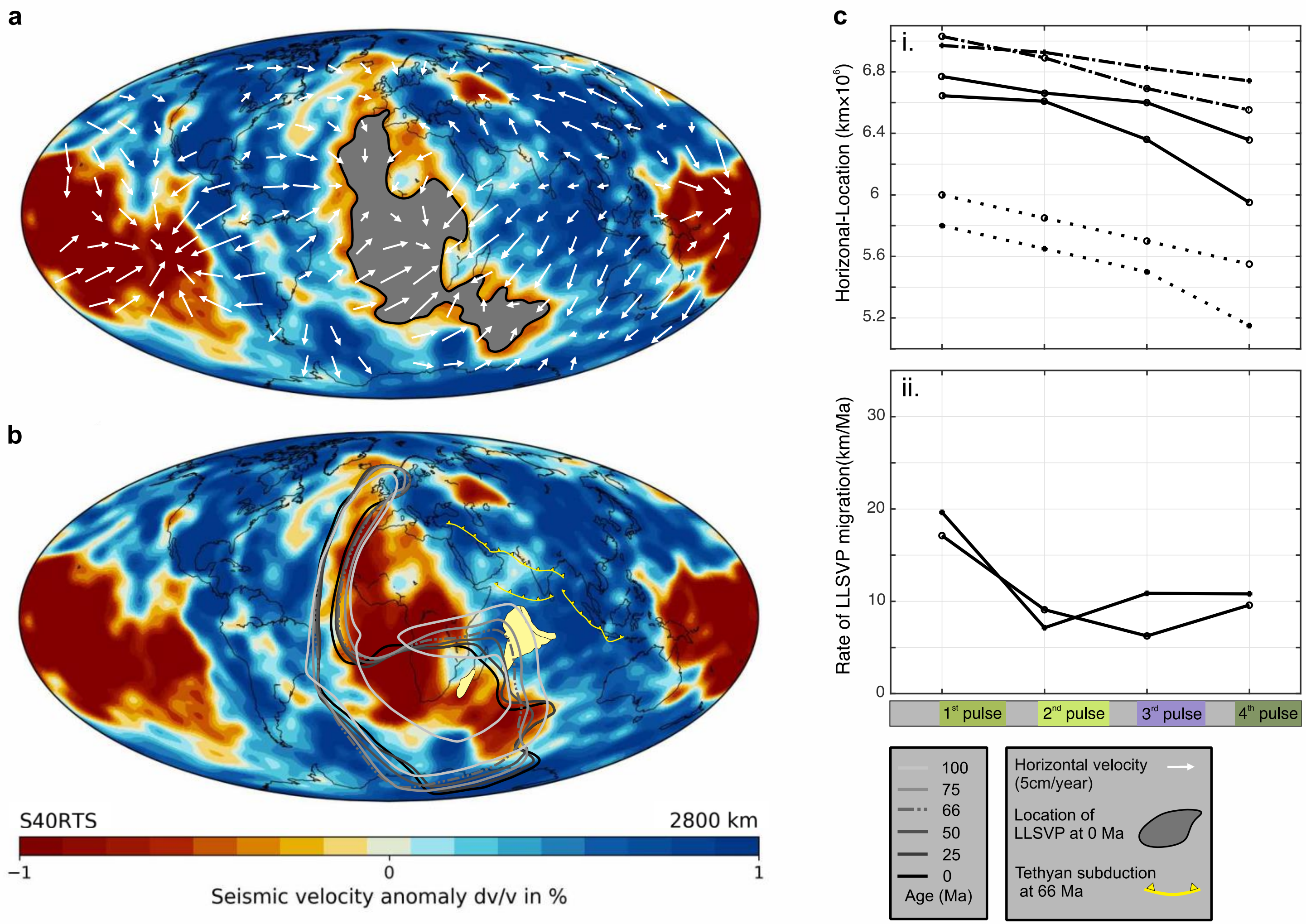

a
b
S40RTS
2800 km
−1
0
1
Seismic velocity anomaly dv/v in %
c
i.
Horizonal-Location (km×10⁶)
6.8
6.4
6
5.6
5.2
ii.
Rate of LLSVP migration(km/Ma)
30
20
10
0
1st pulse
2nd pulse
3rd pulse
4th pulse
100
75
66
50
25
0
Age (Ma)
Horizontal velocity (5cm/year)
Location of LLSVP at 0 Ma
Tethyan subduction at 66 Ma

Figure 8

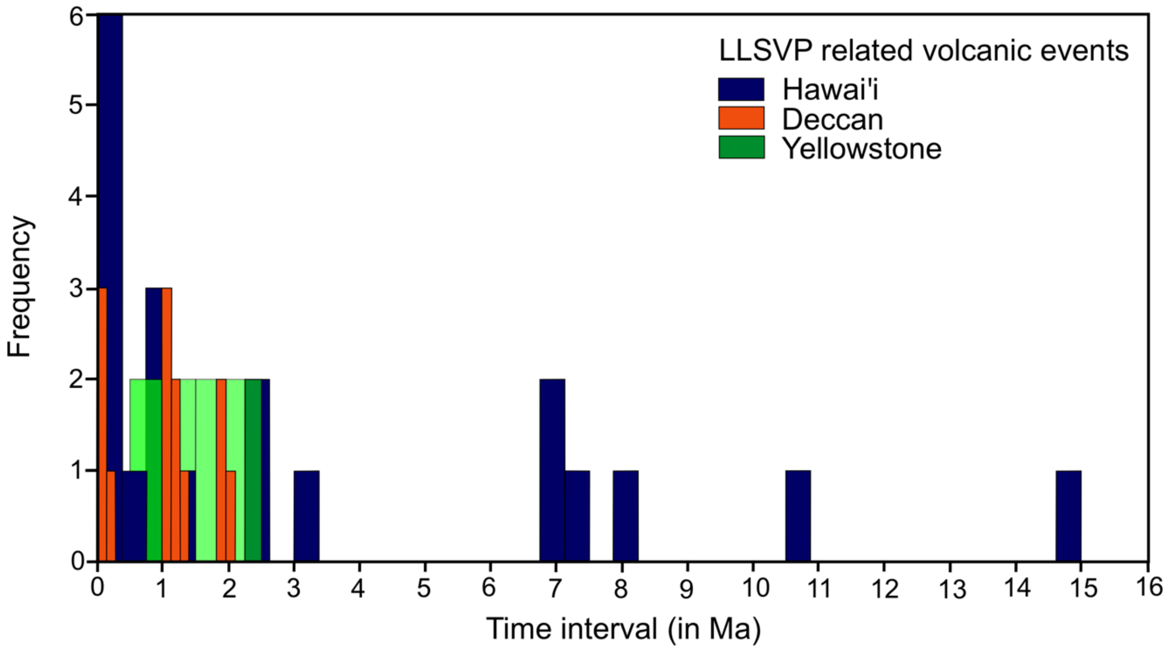
LLSVP related volcanic events
Hawai'i
Deccan
Yellowstone
Frequency
0
1
2
3
4
5
6
0
1
2
3
4
5
6
7
8
9
10
11
12
13
14
15
16
Time interval (in Ma)

Table 1

Physical parameters and their values used for thermochemical modelling

Model Parameters	Reference values
Mantle thickness z_0	2890 km
Reference density ρ_o	3340 kg/m^3
Reference viscosity μ_o	2×10^{21} Pa s
Thermal Viscosity exponent A	4.8
Lower mantle viscosity	6×10^{22} Pa s
Lithosphere viscosity	1×10^{24} Pa s
Compositional viscosity pre-factor $\zeta(\overline{c})$	0.1-100
Thermal conductivity k^*	4.1 W K^{-1}m^{-1}
Specific heat C_P	1250 J K^{-1} kg^{-1}
Thermal expansivity α_0	1×10^{-5} K^{-1}
Thermal boundary layer thickness at the CMB h_{TBL}	100 km
Initial basal layer thickness h_{pile}	150 km
Basal layer density ρ_b	3700-3780 kg/m^3
Basal layer viscosity μ_b	$6 \times 10^{21} - 6 \times 10^{24}$ Pa s
Viscosity ratio $\mu^\dagger$	$0.1 - 10^2$
Top temperature T_{top}	300 K
Bottom temperature T_{bot}	3300 K
Reference Temperature T_0	1600 K
Buoyancy number B	0.6 to 1.4
Background Heating rate X	6×10^{-9} W/m^3
Basal layer heat producing element concentration c_{HPE}	$1\text{X} - 20\text{X}$
Initial basal layer volume‡	3×10^8 km^3
Clapeyron slope at 660 km phase transition γ_{660}	-2×10^6 Pa/K
Density change at 660 km phase transition	200 kg/m^3
Clapeyron slope at 410 km phase transition γ_{410}	3×10^6 Pa/K
Density change at 410 km phase transition	100 kg/m^3

* Thermal diffusivity (κ_0) is calculated in ASPECT from thermal conductivity and it has a value of 10^{-6}

† Ratio of viscosity of the basal layer and the ambience

‡ Initial basal layer volume is calculated from the total volume of African LLSVP considering that the eastern flank (corresponds to the initial basal layer) comprises only a fraction of the total volume.

Table 2

Physical parameters and their values used to model partial melting in plumes

Model Parameters	Reference values
Melt density ρ_f	2700 kg/m^3
Reference shear viscosity η_o	5×10^{18} Pa s
Melt viscosity η_f	10 Pa s
Reference permeability k_0	5×10^{-9} m^2
Reference porosity ϕ_0	0.05
Melt weakening factor α	10
Thermal viscosity exponent β	5
Thermal expansion coefficient $\alpha_{thermal}$	3×10^{-5} K^{-1}
Solid compressibility κ_s	3×10^{-12} Pa^{-1}
Melt compressibility κ_f	3.8×10^{-11} Pa^{-1}
CFL number	1